Contents lists available at ScienceDirect

Materials Today Communications

Unveiling the interplay of deformation mechanisms in a metastable high entropy alloy with tuned composition using synchrotron X-ray diffraction

E. Polatidis [a],[*], S. Shukla [b], J. Čapek [a], S. Van Petegem [c], N. Casati [c], R.S. Mishra [b],[d]

[a] Laboratory for Neutron Scattering and Imaging, Paul Scherrer Institute, PSI, CH-5232 Villigen, Switzerland
[b] Center for Friction Stir Processing, Department of Materials Science and Engineering, University of North Texas, Denton, TX 76207 USA
[c] Laboratory for Condensed Matter Paul Scherrer Institute, PSI, CH-5232 Villigen, Switzerland
[d] Advanced Materials and Manufacturing Processes Institute, University of North Texas, Denton, TX 76203 USA

ARTICLE INFO

ABSTRACT

The mechanical behavior of a metastable high entropy alloy (HEA) with composition Fe39-Mn20-Co20-Cr15-Si5-1Al at% is investigated. The deformation mechanisms contributing to its mechanical properties are unveiled, by performing uniaxial tensile tests in situ with synchrotron X-ray diffraction. Three distinct deformation regimes are detected. The initial elastic and early dislocation-based plasticity deformation is followed by a moderate work hardening rate regime, which is associated with the deformation-induced phase formation of ε-martensite, with hexagonal close-packed (hcp) crystal structure as well as slip in the parent austenitic phase. During the third deformation regime, the phase transformation continues to occur in combination with 2 modes of hcp twinning as well as slip in the unfavorably oriented grains for twinning. The interplay of all these co-existing deformation mechanisms can be evidenced by synchrotron X-ray diffraction.

1. Introduction

High Entropy alloys (HEAs) were first introduced in 2004 [1,2] as alloys having at least five principal elements in or near equi-atomic compositions. The rationale behind the HEA design concept is the usually high entropy of mixing. HEAs are characterized by a stable solid solution-based alloy with high hardness, strength and stability at high temperature. Based on the equimolar alloy designed by Cantor et al. [2], variants with modified compositions or non-equimolar compositions have been developed, to reduce the stacking fault energy of the system and promote twinning induced plasticity (TWIP) and/or the transformation-induced plasticity (TRIP), the so-called metastable HEAs. As such materials with superior mechanical properties have emerged. Another strengthening mechanism for HEAs is the addition of nitrogen via the interstitial strengthening effect [3,4].

Metastable HEAs have shown to be able to overcome the work hardening deficiency of conventional HEAs, by fine-tuning the composition allowing the destabilization of the γ-fcc phase (with face-centered cubic crystal structure) [5–12]. Hence, during deformation, ε-hcp forms (with hexagonal close packed crystal structure), which is known as the TRIP effect and hence these alloys are referred as TRIP-HEAs. Recent studies on tailoring the metastability of a TRIP-HEA with a composition

of Fe40-Mn20-Co20-Cr15-Si5 (at%) resulted in responsive microstructural evolution upon friction stir processing (FSP) and an excellent strength and ductility relationship [13–15]. FSP is used for engineering the microstructure since it is a unique process wherein all processing parameters (strain, strain rate, time and temperature) can be controlled simultaneously without changing the cross-section of the material [16]. The remarkable mechanical properties of this alloy are attributed to the synergetic interaction of slip in the parent γ-fcc and, predominantly, the deformation twinning in the product ε-hcp upon deformation [15,17]. The addition of 1 at% Al in this system, followed by FSP, and by subsequently applying annealing treatment was seen to result also in remarkable mechanical properties [18]. It is known that Al is an austenite stabilizer and suppresses the formation of ε-hcp [19], however annealing was shown to result in Al-segregation, from the matrix towards the grain boundaries, resulting in the destabilization of the austenite matrix [18]. Although the destabilization of austenite and the formation of deformation-induced hcp martensite have been observed *ex situ* [18], no detailed investigation was undertaken following the formation of ε-hcp and the subsequent deformation mechanisms upon further straining. Moreover, the sequence of activation of different deformation mechanisms in this system, has never been studied in detail.

---

* Corresponding author.
  E-mail address: efthymios.polatidis@psi.ch (E. Polatidis).

A key aspect of the enhanced ductility and strength in HEAs is the deformation of ε-hcp [20,21] as metals/alloys with hcp crystal structure can exhibit a complex interplay of deformation mechanisms. Yoo in an extensive review in [22] suggested that dislocation slip with a Burgers vector <c+a> is an essential deformation mechanism and alone can be more effective in satisfying compatibility conditions than several twinning systems together [22]. As such promoting more slip modes over basal slip or twinning, which are the most dominant deformation mechanisms in hcp [23], is key in designing more strong and ductile HEAs.

Diffraction methods can be very useful for investigating the complex deformation behavior in multiphase materials because they can offer i) the phase fraction along the deformation process, ii) the lattice strain evolution related to the load sharing between different phases, where the lattice strain ε_{hkl} is determined by the relative change of the interplanar lattice spacing d_{hkl} with respect to d_{0hkl}, which is the initial value prior to deformation of a *hkl* family of lattice planes. iii) the change of integrated intensities between different grain families to study the texture evolution and iv) the diffraction peak broadening which during deformation can result from: i) dislocations and/or elastic strain gradients (type-III strains) and ii) distribution of intergranular strains within a grain family (type-II strains) iii) decrease of the coherent diffraction domain size [24]. Broadening due to crystallite size effects is not expected to be significant in this study. Here, we utilize in situ synchrotron X-ray diffraction in transmission geometry during uniaxial tensile deformation of a metastable Fe39-Mn20-Co20-Cr15-Si5-Al1 (at%) HEA to study the evolution of the TRIP effect and the interplay of deformation mechanisms. Post-mortem EBSD is performed to verify some of the observations of the synchrotron XRD investigation.

2. Experimental

A HEA with a nominal composition of Fe39-Mn20-Co20-Cr15-Si5-Al1 (at%) was produced by vacuum arc casting in a cold copper crucible with a size of $300 \times 100 \times 6$ mm^3 in Ar atmosphere. The ingot was subsequently friction stir processed (FSP) using a W–Re tool for 2 passes; more details are given in [18]. Stripes of 0.3 mm in thickness were cut along the FSP line using electrical discharge machining. Miniaturized dogbone samples were cut using a picosecond laser at the Swiss Federal Laboratories for Materials Science and Technology (EMPA), in Switzerland. More details on the sample geometry and fabrication are given in [25]. The dogbone samples were annealed at 650 °C for 30 min, then cooled in air. After annealing, a limited grain growth is observed, in agreement with [18], i.e. the average grain size increases from 0.8 μm with 0.8 μm standard deviation to 1.1 μm with 0.9 μm standard deviation before and after annealing respectively, excluding the annealing twins which are present in both conditions. The dogbone samples were then ground and polished down to approximately 0.1 mm thickness so that X-rays can penetrate through the sample. For the initial and post-deformation characterization of the microstructure by electron backscatter diffraction (EBSD), small pieces of the as-annealed material and deformed material were mechanically polished with SiC papers up to 4000 grit and electropolished using a 16:3:1 (by volume) ethanol, glycerol and perchloric acid solution at 48 V for 10 s. A field emission gun scanning electron microstructure (FEG SEM) Zeiss ULTRA 55 equipped with EDAX Hikari Camera operated at 20 kV in high current mode with 120 μm aperture was used. The acquired EBSD raw data were post processed using the EDAX OIM Analysis 7.3 software and MTEX open source toolbox [26].

The "mesobiaxial" tensile machine described in [27] was mounted on the goniometer of the Materials Science (MS) X04SA beam line at the Swiss Light Source (SLS). The deformation test was undertaken in displacement control with 0.6 μms^{-1} displacement rate (i.e. 2×10^{-4} s^{-1} strain rate). The total strain was measured assuming that the displacement is concentrated at the gauge length of the dogbone sample, where the displacement of the grips is recorded by piezo sensors on the mesobiaxial machine. The diffraction experiment was carried out in transmission mode using a Pilatus 6 M detector, at 25 keV and 70×70 μm^2 beam spot-size probing the center of the dogbone. The diffraction measurements were obtained continuously during loading/unloading with 5 s acquisition time per diffraction pattern. A LaB$_6$ NIST SRM 660b standard was used as reference for calibrating the diffraction setup using FIT2D [28]. The 2D diffraction images were caked and integrated using FIT2D along an azimuthal range of 85–95° and 265–275° corresponding to the loading direction (LD) and 355–5° and 175–185°, corresponding to the transverse direction (TD). Single-peak fitting was undertaken with a pseudo-Voigt function using an in-house developed MATLAB code. Rietveld refinement was undertaken with GSAS-II [29] by integrating every diffraction image along the entire azimuthal range of 360° and along the deformation test. Starting from the last histogram (i.e. at the highest strain), and after refining the lattice parameters of γ-fcc and the ε-hcp phases, the phase fraction was refined. Then, a cylindrical symmetry texture model using a 12 and 9 harmonic order for the γ-fcc and ε-hcp phase respectively was used to model the crystallographic texture. An isotropic microstrain model was used for modeling the peak broadening in both phases. The background was fitted using a Chebyshev polynomial of 6 orders. The backward sequential refinement (towards lower true strain) of all data was undertaken by refining the phase fraction, the microstrain model, the texture, and Hydrostatic/elastic strain to capture the lattice strain. The maximum number of refinement cycles was set to 10 and the refined parameters were propagating to the next histogram. Two diffraction patterns and the refined patterns are exemplarily shown in Fig. 1. The goodness indicators of for the γ-fcc and the ε-hcp phases were sufficient and the obtained phase fraction values exhibit low uncertainty.

3. Results

The initial microstructure shows small equiaxed austenitic grains with relatively random crystallographic texture, as shown in Fig. 2a. The indexed microstructure is 100% austenitic as shown in Fig. 2b.

During the deformation of the TRIP-HEA, three work hardening rate (WHR) regimes are observed as shown in Fig. 3. After the initial elastic response with the macroscopic yield stress being at around 350 MPa and up to 5% (applied) true strain, the WHR-I regime is observed. Then, up to approximately 23% (applied) true strain, a less steep decreasing WHR is observed, i.e. WHR-II; while a stronger change of in the slope of the WH is observed at (applied) true strains above 23%, i.e. the WHR-III where the work hardening rate changes and further increases. This change in the WHR is indicative of a possible change in the dominant deformation mechanisms [30,31] or to a change in balance between deformation mechanisms [32].

The evolution of the phase fraction of the deformation-induced ε-hcp is shown in Fig. 4. A small detectable fraction of ε-hcp was revealed by synchrotron X-ray diffraction in the as-annealed state. The deformation-induced phase transformation starts at approximately 5% (applied) true strain, which coincides with the onset of WHR-II. The onset of WHR-II is hence attributed to the formation of ε-hcp plates acting as effective barriers to the dislocation motion within γ-fcc. Furthermore, the creation of phase boundaries was seen to induce defects in order to ensure lattice continuation, hence excess dislocations are generated, the so-called geometrically necessary dislocations, which locally strengthen the material [33]. The phase transformation continues throughout the deformation test and by the end of it approximately 88% of ε-hcp is formed, which is in agreement with the post-deformation EBSD shown in Fig. 5, where pockets of retained austenite are observed after the deformation. The retained austenite has a relatively strong < 100 > texture along the LD as shown in Fig. 5c where the IPF intensity close to the < 100 > orientation is ~2.8 times random. The creation of strong < 100 > texture along the LD is attributed to the deformation texture but meanwhile indicative of the resistance to the TRIP effect within {100} grains aligned with the lLD [34,35].
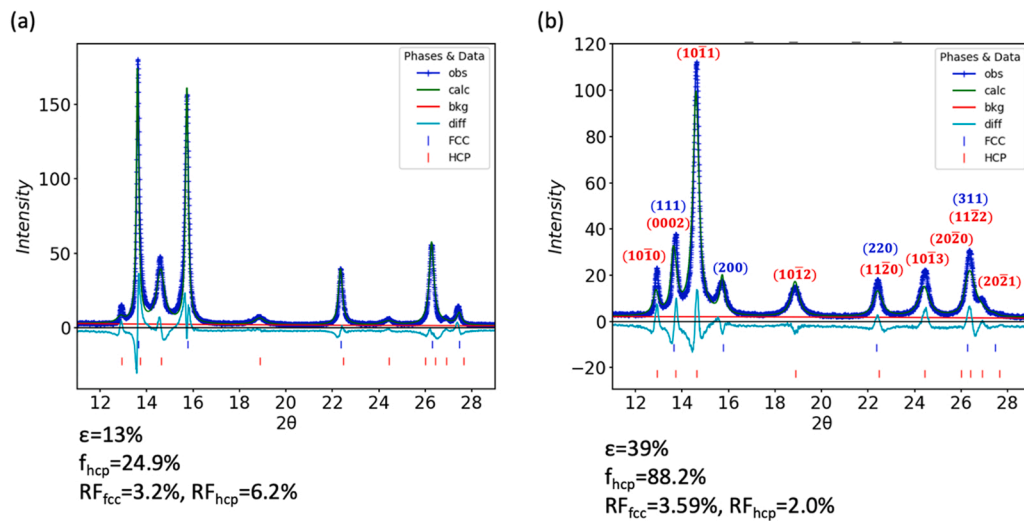
(a)

ε=13%
f_hcp=24.9%
RF_fcc=3.2%, RF_hcp=6.2%

(b)

ε=39%
f_hcp=88.2%
RF_fcc=3.59%, RF_hcp=2.0%

Fig. 1. Examples of Rietveld refinement profiles at two different (applied) true strains (ε), showing the calculated fraction of ε-hcp (f_hcp) and the goodness of fit RFfcc and RFhcp for the γ-fcc and ε-hcp phases respectively. The fcc diffraction peaks are indexed with blues color and the hcp diffraction peaks with red (obs=experimental data, calc=fitted, bkg=fitted background, diff=difference between calc+bkg and obs). (For interpretation of the references to colour in this figure, the reader is referred to the web version of this article)
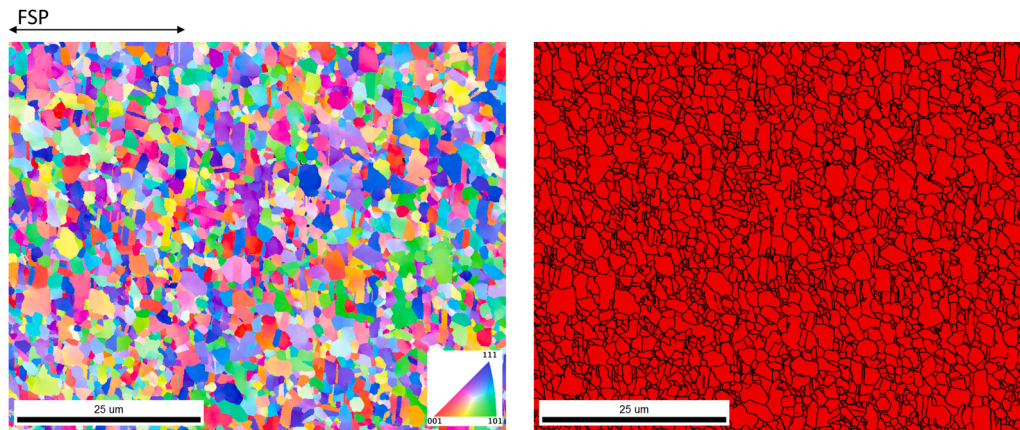

Fig. 2. (a) Orientation map with IPF coloring of the undeformed material in the out-of-plane direction. (b) Phase map showing the initial microstructure indexed as only austenite (red color). The FSP direction is indicated by a double arrow. (For interpretation of the references to colour in this figure, the reader is referred to the web version of this article)
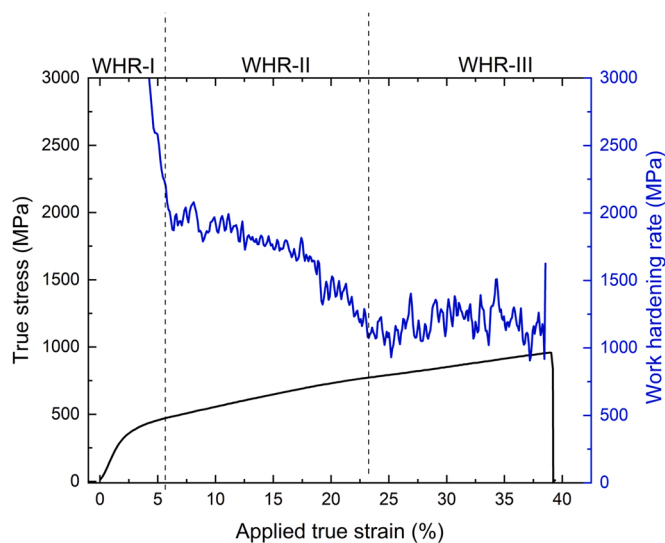

Fig. 3. True stress vs. applied true strain and WHR curves of Al-HEA annealed at 650 °C for 30 min.§
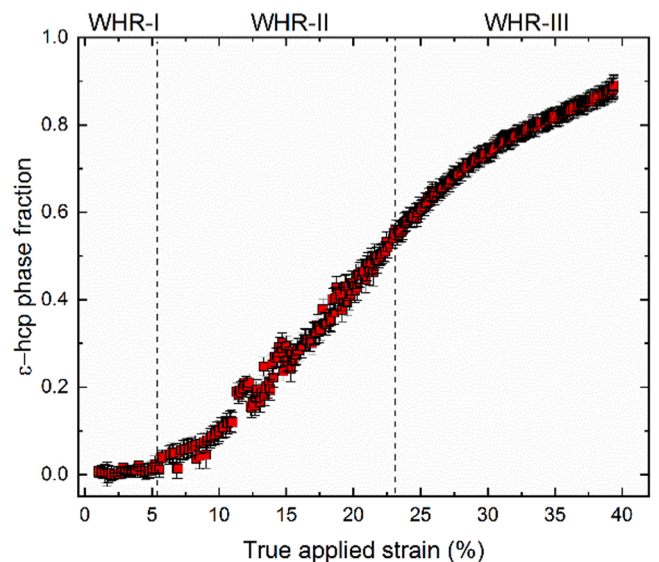

Fig. 4. The evolution of deformation-induced phase transformation, obtained from the Rietveld refinement.
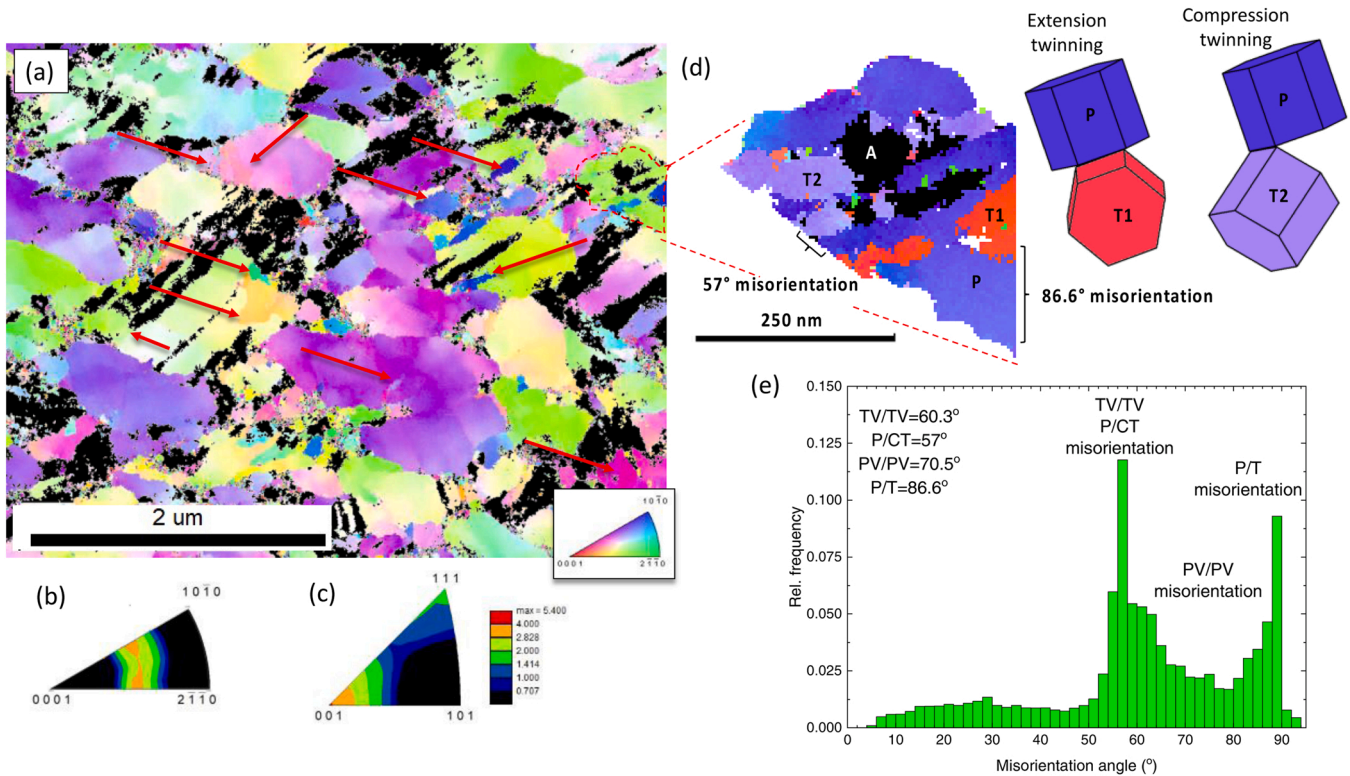
Fig. 5. (a) Orientation map with IPF coloring of the deformed material in the LD for the ε-hcp phase. Austenite is shown with black. The red arrows indicate ε-hcp extension twin-boundaries. (b) IPF of the ε-hcp phase and (c) γ-fcc in the LD after deformation at 38% (applied) true strain, showing the strong texture that evolves in the [100] direction. (d) A close-up of an ε-hcp grain from (a) with IPF coloring in the out-of-plane direction, containing traces of austenite (A) shown in black color, a parent ε-hcp grain (P) which has 86.6 degrees misorientation with respect an extension twin variant (T1), while compression twin variant (T2) appears with 57 degrees misorientation. The unit cells and the orientation relationship between P, T1 and T2 are shown schematically. (e) Histogram showing the misorientation between grain boundaries exhibiting two distinct peaks for grain boundaries at ~60 and ~90 degrees due to i) boundaries between deformation-induced parent ε-hcp with compression twins (P/CT with 57 degrees misorientation) and different ε-hcp extension twin variants (TV/TV with 60.3 degrees misorientation) ii) boundaries between deformation-induced parent ε-hcp grains and extension twins (P/T with 86.6 degrees misorientation), respectively. The IPFS and the histogram are obtained after merging 3 EBSD maps as the one shown in (a) for improved grain statistics. (For interpretation of the references to colour in this figure, the reader is referred to the web version of this article)

Early during the WHR-I regime, the strain is accommodated elastically in both phases, as seen by the linear increase in the lattice strain in Fig. 6. Specifically, even before the macroscopic yield stress, (i.e. at 350 MPa), the lattice strain accumulation slows down for the {111} and {311} γ-fcc lattice plane families. In addition, part of the load is shed to the {200} lattice plane family, which continues to accumulate

significant load at an increased rate. This observation agrees well with previous diffraction studies where the {200} lattice plane family shares significant load above the macroscopic yielding point [36,37].

In addition to γ-fcc, significant load is shared by ε-hcp, as shown in Fig. 6b where the evolution of lattice strain of the {10$\bar{1}$0}, {10$\bar{1}$1},
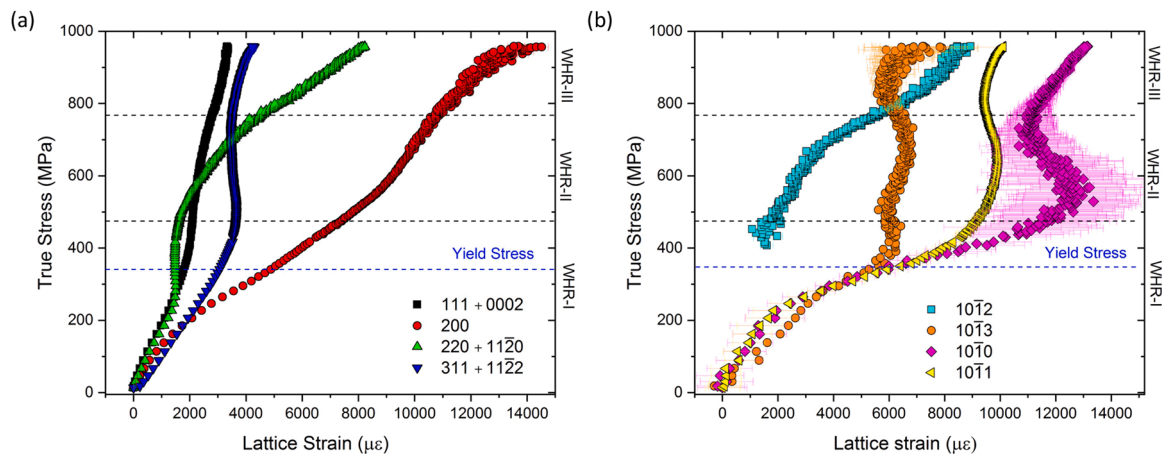

Fig. 6. (a) Lattice strain evolution with true stress along the LD for the {111}, {200} and {311} γ-fcc lattice plane families. (b) Lattice strain evolution for the {10$\bar{1}$0}, {10$\bar{1}$1} and {10$\bar{1}$2} ε-hcp lattice planes families. The {10$\bar{1}$2} peak was not visible before plastic deformation when new deformation-induced transformation occurred.

{10$\bar{1}$2} and {10$\bar{1}$3} families of lattice planes is presented. It is seen that after the initial elastic loading, as apparent by the linear increase of the lattice strain up to approximately 300 MPa, the lattice strain increases significantly in ε-hcp. Note that beyond the yield point and as ε-hcp forms, the (111), (220) and (311) diffraction peaks overlap with the (0002), (11$\bar{2}$0) and (11$\bar{2}$2) diffraction peaks of ε-hcp respectively (cf. Fig. 1b) and therefore the evolution of lattice strain for the corresponding lattice plane families, cannot be reliably interpreted. Close to the onset of the deformation-induced transformation, the lattice strain of the (10$\bar{1}$1) and (10$\bar{1}$3) diffraction peaks becomes almost vertical, which indicates that nearly perfect plastic deformation in these grain families occurs. Note that the family of planes that plasticity appears to occur earliest (at around 380 MPa) is (10$\bar{1}$3). In contrast to the plastically deformed lattice plane families, the {10$\bar{1}$0} lattice plane family sheds some load to the {10$\bar{1}$2}. The lattice strain further increases for almost all lattice plane families during the WHR-III, due to twinning which will be discussed in the next paragraphs. The significant lattice strain in the pyramidal {10$\bar{1}$1} lattice plane family has been previously observed and it was attributed to the activation of pyramidal <a> and <c+a> slip [17,38]. The slip activity in the {10$\bar{1}$1} lattice plane family is discussed in Section 4.

Fig. 7a and Fig. 7b show the evolution of the integrated diffraction intensity (normalized by the highest integrated diffraction intensity of each diffraction peak) of several diffraction peaks for both γ-fcc and ε-hcp, in the direction parallel to the LD. All γ-fcc diffraction peaks exhibit an overall decrease in intensity, due to predominantly the phase transformation, however, the change is not easily interpretable quantitatively, due to the overlap of γ-fcc and ε-hcp diffraction peaks (see Fig. 7a). In addition, due to the strong overlap of the fcc and hcp diffraction peaks, a reliable interpretation of the FWHM or quantitative line broadening analysis on the type or density of dislocations, throughout the deformation, is not possible. The evolution of the integrated diffraction intensity of the (200) diffraction peak which does not overlap with any ε-hcp diffraction peak is understood as follows: during the initial deformation, up to 5% (applied) true strain, a slight increase is observed due to the deformation texture, i.e. relatively strong < 100 > texture forms in the LD in fcc materials during dislocation plasticity [39]. After the yield point, the fcc diffraction peak width increases which is indicative for increase in dislocation density, as shown in Fig. 8. From 5% (applied) true strain, the integrated diffraction intensity decreases as γ-fcc is partially consumed for the formation of ε-hcp.

The integrated diffraction intensity of the {10$\bar{1}$1}, {10$\bar{1}$2} and {10$\bar{1}$3} peaks of the ε-hcp phase exhibit initially an increase with strain,
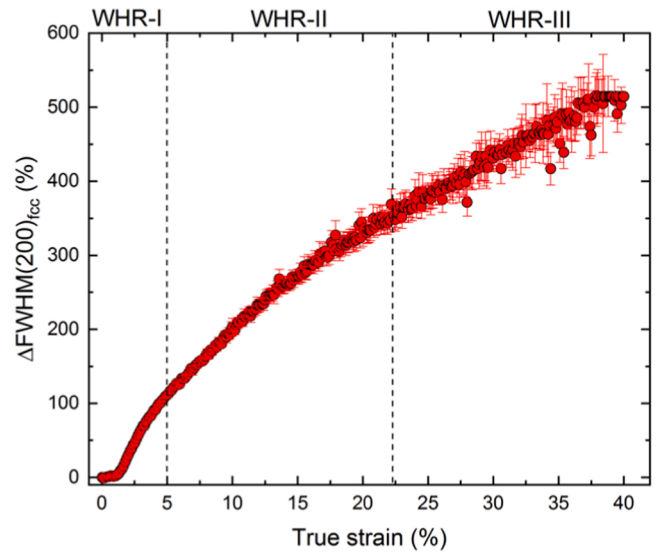

Fig. 8. Evolution of the change of the full-width-at-half maximum (FWHM) of the (200) fcc diffraction peak with respect to its initial FWHM.

due to the increasing fraction of ε-hcp, as shown in Fig. 4. The {10$\bar{1}$2} and {10$\bar{1}$3} grain families, together with {0002} in the LD, have relatively high Schmid factor for extension twinning [40]. It should be noted that the intensity change in the (0002) lattice plane family imposed by possible twinning cannot be reliably followed due to strong overlapping with the (111) and diffraction peak of the γ-fcc phase. The integrated diffraction intensity of the {10$\bar{1}$2} and {10$\bar{1}$3} initially increases due to the formation of ε-hcp, but close to the onset of the WHR-III, they strongly decrease in the LD, meanwhile the integrated intensity of these diffraction peaks increases significantly in the TD, as shown in Fig. 7 and in Fig. 8. Such re-orientation is characteristic of {10$\bar{1}$2}⟨10$\bar{1}$1⟩ extension twinning, i.e. a 86.6° rotation from the LD to the TD which has been previously observed by neutron or synchrotron X-ray diffraction studies [17,41,42] or by EBSD [17,43]. The presence of several twins in the deformation-induced ε-hcp phase is evidenced by EBSD in the post-deformed state as shown in Fig. 5e. The histogram shown in Fig. 5e shows a peak at misorientations of approximately 90 degrees, which corresponds to the existence of twins in the deformation induced ε-hcp grains, as such the parent/twin ε-hcp interface is associated with a 86.6 degrees misorientation. It is also evidenced that another peak occurs at misorientations of around 60 degrees, which corresponds to the
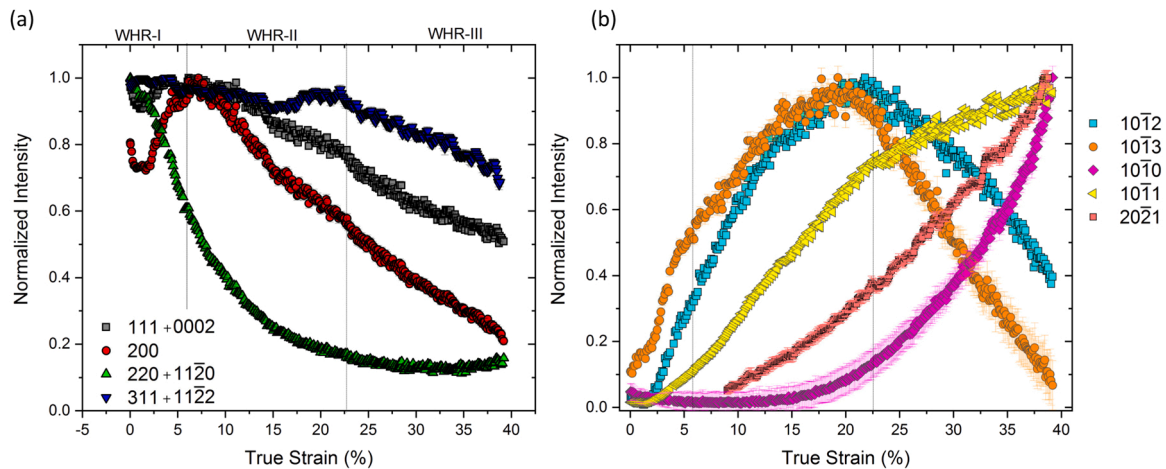

Fig. 7. Evolution of the integrated intensity of the a) (111)+ (0002), (200), (220)+ (11$\bar{2}$0) and (311)+ (11$\bar{2}$2) and b) (10$\bar{1}$0), (10$\bar{1}$1), (10$\bar{1}$2) and (10$\bar{1}$2) ε-hcp diffraction peaks along the LD.

formation of compression twins $\{10\bar{1}1\}\langle10\bar{1}2\rangle$ with 57 degrees misorientation with respect to their parent ε-hcp grain and the coexistence of several extension twin variants which grow and impinge each other, sharing grain boundaries close to the characteristic misorientation of 60.3 degrees (Fig. 5d). Such peaks indicating the presence of several twin/twin and parent ε-hcp/twin boundaries have been also observed in Mg alloys [44]. Finally, an increased frequency in misorientations occurs at angles of around 70 degrees, which most probably corresponds to the growth and impingement of different deformation induced ε-hcp variants in the parent γ-fcc.

It is also observed in Fig. 5b that in the deformed state, the microstructure contains strong $\{10\bar{1}1\}//LD$ texture in agreement with the previous observation of strongly textured deformation-induced ε-hcp in HEAs [45]. The $\{10\bar{1}1\}$ lattice plane family has low SF for deformation twinning and as observed in Fig. 5, such grains shown in purple IPF colouring in the LD, contain very small twins or no twins at all. It is also interesting to note that twinning occurs first in the $\{10\bar{1}3\}$ grains and later in the $\{10\bar{1}2\}$ grains, as apparent by the change of integrated diffraction intensity at different strains in Fig. 7b. This is expected, considering that the critical resolved shear stress (CRSS) is the same for the same twinning system for all grain families, while the Schmid Factor for extension twinning for the $\{10\bar{1}3\}$ and the $\{10\bar{1}2\}$ grains is 0.34 and 0.23 respectively; hence twinning starts earlier in the $\{10\bar{1}3\}$ grains. Simultaneously, as a most preferable product of tensile twinning, the intensity of the $(10\bar{1}0)$ diffraction peak increases in the LD [46]. It is also noted that the intensity of the $(20\bar{2}1)$ diffraction peak increases by tensile twinning, while its parent, the $\{4\bar{1}\bar{2}4\}$ family of planes [46]; is not observed as it is outside the detection range of the detector.

4. Discussion

The evolution of the integrated intensity of specific ε-hcp diffraction peaks with strain and how it is distributed between the LD and TD can reveal the deformation mechanisms. In contrast to neutron diffraction featuring only 2 detector banks with limited angular coverage [17], XRD utilizing a 2D detector in transmission provides information on the azimuthal distribution of diffraction intensity as shown in Fig. 9. This is particularly useful for the interpretation of the deformation mechanisms of this material. For instance, the integrated intensity of an ε-hcp diffraction peak can change with increasing strain due to i) more deformation-induced ε-hcp transformation leading to an increase of the intensity and/or ii) texture change due to deformation-induced twinning and/or dislocation slip both leading to either increase or decrease of the diffraction intensity depending on the diffraction peak and the slip/twinning mechanism. In the latter case, twinning results in characteristic re-orientation of specific lattice planes families from the LD to the TD or vice versa, which depends on the twinning mode. In contrast, dislocation slip results in distributing the diffraction intensity along a range of azimuthal angles caused by crystallographic misorientation distribution within the grains caused by slip [47]. Based on the X-ray diffraction results and the accompanying EBSD results, the following deformation mechanisms can be revealed for each deformation stage.

4.1. WHR-I

The WHR-I regime is associated with plasticity in the two phases, as apparent by the deviation of the lattice strain from linearity which are shown in Figs. 6a and 6b as well as the increase of the FHWM of the (200) fcc diffraction peak shown in Fig. 8. No transformation is observed during this deformation stage as shown in Fig. 4.

4.2. WHR-II

The WHR-II regime is associated with the formation of ε-hcp as shown in Fig. 4. Based on the diffraction intensity evolution shown in
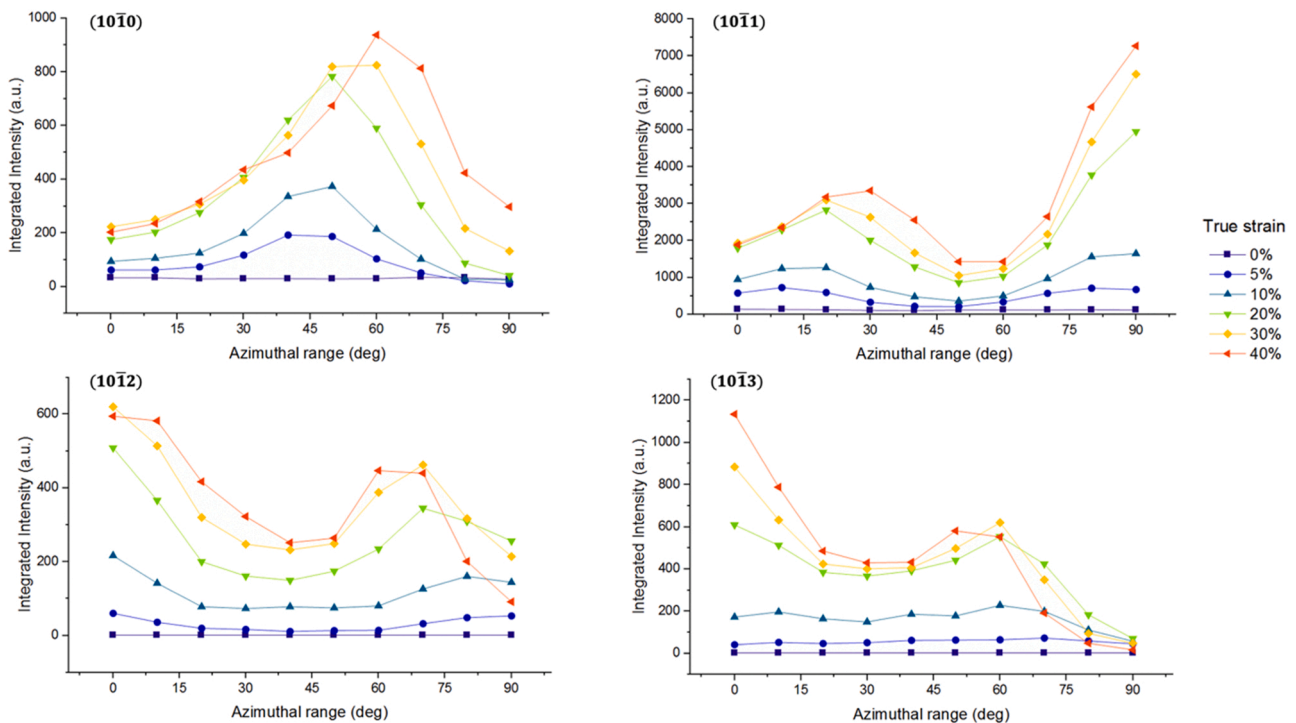

Fig. 9. Evolution of the integrated intensity of the $(10\bar{1}0)$, $(10\bar{1}1)$, $(10\bar{1}2)$ and $(10\bar{1}3)$ diffraction peaks with strain at azimuthal ranges from the LD (90°) to the TD (0°) with 5° azimuthal binning. $(10\bar{1}0)$: relatively strong texture. The intensity "peak" gradually spreads over a wider range of azimuthal angles, indicative of dislocation slip. $(10\bar{1}1)$: relatively strong crystallographic texture (strong azimuthal variation) already at 5% and at 10% strain. The intensity growth slows down and spreads over a range from 90° to 60° at strains above 20%. $(10\bar{1}2)$ and $(10\bar{1}3)$: typical behavior of extension twinning; the intensity decreases in the LD and it increases in the TD at strains above 20%, i.e. a nearly 90° rotation due to twinning.

Fig. 7b, twinning appears to be triggered at (applied) true strain higher than 15% and extension twins form in the $\{10\bar{1}2\}$ and $\{10\bar{1}3\}$ grain families towards the end of WHR-II. As a result of extension twinning strong reorientation of the $\{10\bar{1}2\}$ and $\{10\bar{1}3\}$ grains is observed towards the TD (Fig. 9), which is also verified by the post-mortem EBSD in Figs. 5a and 5e. Besides the apparent twinning in these grain families, it is expected that other grain families (e.g. the basal $\{0002\}$ family which exhibits the highest Schmid factor) should also exhibit pronounced extension twinning although, they cannot be revealed due to strong overlapping of the diffraction peaks with the fcc diffraction peaks.

4.3. WHR-III

The WHR-III regime is associated with continuous formation of ε-hcp and extension twinning in the $\{10\bar{1}2\}$ and $\{10\bar{1}3\}$ grain families. Meanwhile, the increase in the diffraction intensity of the $\{10\bar{1}1\}$ grain family, which dominates the crystallographic texture in the LD, slows down as shown in Fig. 7b. The $\{10\bar{1}1\}$ grain family exhibits limited extension twinning as shown in Fig. 5. Based on the intensity evolution in Fig. 7 and the azimuthal diffraction intensity distribution in Fig. 9, these grains exhibit more pronounced slip; the type of slip is discussed in the following paragraphs. As a results of enhanced twinning, the macroscopic work hardening rate exhibits a deflection point (as shown in Fig. 3). There have been numerous studies addressing the complex effect on twinning on the macroscopic strain hardening. It has been reported that twinning predominantly results in hardening, due to Hall–Petch grain size strengthening. The formation of twin boundaries appear to reduce the effective grain size [48,49]. Besides the presence of twin boundaries, Basinski et al. have proposed an additional hardening mechanism by the transformation of glissile dislocations into sessile configurations by twinning [50] or high density of geometrically necessary dislocations have been observed at the twin boundaries [51].

A recent investigation on a metastable Fe50-Mn30-Co10-Cr10 (at%) HEA, postulated the dominance of deformation twinning, because the diffraction intensity of the $(10\bar{1}1)$ diffraction peak grows during deformation in the LD [41]. In contrast, for the material studied here, the growth of the diffraction intensity of the $(10\bar{1}1)$ diffraction peak during the WHR-III regime slows down, as shown in Fig. 7b, although the transformation continues to occur as shown in Fig. 4. A decrease in the diffraction intensity of the $(10\bar{1}1)$ diffraction peak along the LD has been observed in [46,52] and modelled in [53,54] and it has been attributed to dominating pyramidal <c+a> dislocation slip in Mg alloys [53]. Furthermore, the EBSD map in Fig. 5 shows that the grains close to the $\{10\bar{1}1\}$ texture do not exhibit pronounced twinning but show color variations due to the slip activity and misorientation caused by it. A further justification of enhanced slip activity is seen in Fig. 9: early during deformation, i.e. 5–10% (applied) true strain, the intensity of the $(10\bar{1}1)$ diffraction peak shows already variations along the azimuthal range from LD to TD, due to strong crystallographic texture, i.e. relatively strong $\{10\bar{1}1\}$ texture forms parallel to the LD as shown in Fig. 9. By increasing the applied strain, the diffraction intensity is distributed in a range of azimuthal angles, close to the LD, caused by the misorientations imposed by the slip activity. All these observations suggest that the $\{10\bar{1}1\}$ plane family which dominates the microstructure in the LD (Fig. 5b), exhibits more slip than twinning activity.

The crystallographic axial ratio, c/a, of the hexagonal unit cell, where a is the lattice constant of the basal axis and c is the lattice constant of the prismatic axis, determines the activation of different deformation mechanisms as it affects the CRSS of the different systems [55]. Hence it has been observed that systems with a CRSS ratio between basal and no basal slip, close to 1, exhibit both basal and non basal slip [56]. As such HEAs are ideal systems for modifying the c/a ratio through alloying and hence for engineering their mechanical properties by promoting the most appropriate deformation mechanisms [38,43]. The c/a

ratio, as obtained from the Rietveld refinement, remains below the ideal value of 1.633 (the ideal value obtained for close packing of hard spheres [55]) during the entire deformation process, i.e. the c/a is 1.615 ± 0.01 during the entire deformation process, which is in agreement with [43]. Based on an extensive investigation on the deformation mechanisms in HEAs using transmission electron microscopy (TEM) in [38], significant non basal <c+a> slip was observed in systems with c/a ratio of 1.615. Furthermore, in a systematic investigation in [43], it was shown that the addition of austenite stabilizers (e.g. Cu and Al) reduces the c/a ratio. Based on the above, the HEA studied here, has a low enough c/a ratio that promotes <c+a> slip in the pyramidal $\{10\bar{1}1\}$ planes. Employing TEM for revealing the type of dislocation activity in the ε-hcp phase is beyond the scope of this work as it is local, whereas, synchrotron XRD itself can reveal the characteristics associated with specific deformation mechanisms and their relation to changes in the observed macroscopic mechanical behavior the material.

5. Conclusions

In conclusion, in situ deformation and synchrotron X-ray diffraction in transmission geometry can reveal the characteristics of the interplay of deformation mechanisms in a Fe39-Mn20-Co20-Cr15-Si5-Al1 HEA. It is observed that a synergy of deformation mechanisms is operational during the course of deformation and they are accompanied by changes in the work-hardening rate of the material. In addition to dislocation slip in the γ-fcc phase, the onset of the TRIP effect is associated with change in the work hardening rate. The next work hardening rate change is associated with twinning in the $\{10\bar{1}2\}$ and $\{10\bar{1}3\}$ grain families of the deformation-induced ε-hcp phase. Meanwhile suppression of deformation twinning is observed in the $\{10\bar{1}1\}$ grain family, which dominate the crystallographic orientation along the loading direction. Apparent pronounced slip activity which is associated with the relatively low c/a ratio of the strain-induced ε-hcp phase, reducing the CRSS for non-basal slip, is evidenced by X-ray diffraction in the $\{10\bar{1}1\}$ grain family. In addition to extension twinning, post-mortem EBSD verifies the existence of compression twinning in the ε-hcp phase.

CRediT authorship contribution statement

E. Polatidis: Conceptualization, Data curation, Formal analysis, Investigation, Writing – original draft, Writing – review & editing. **S. Shukla:** Conceptualization, Investigation, Writing – review & editing. **J. Čapek:** Data curation, Formal analysis, Investigation, Writing – review & editing. **S. Van Petegem:** Data curation, Investigation, Methodology, Writing – review & editing. **N. Casati:** Methodology, Writing – review & editing. **R.S. Mishra:** Conceptualization, Writing – review & editing.

References

[1] J.-W. Yeh, S.-K. Chen, S.-J. Lin, J.-Y. Gan, T.-S. Chin, T.-T. Shun, C.-H. Tsau, S.-Y. Chang, Nanostructured high-entropy alloys with multiple principal elements: novel alloy design concepts and outcomes, Adv. Eng. Mater. 6 (2004) 299–303, https://doi.org/10.1002/adem.200300567.

[2] B. Cantor, I.T.H. Chang, P. Knight, A.J.B. Vincent, Microstructural development in equiatomic multicomponent alloys, Mater. Sci. Eng. A 375–377 (2004) 213–218, https://doi.org/10.1016/j.msea.2003.10.257.

[3] M. Ojima, Y. Adachi, Y. Tomota, K. Ikeda, T. Kamiyama, Y. Katada, Work hardening mechanism in high nitrogen austenitic steel studied by in situ neutron diffraction and in situ electron backscattering diffraction, Mater. Sci. Eng. A 527 (2009) 16–24, https://doi.org/10.1016/j.msea.2009.07.066.

[4] Y. Han, H. Li, H. Feng, K. Li, Y. Tian, Z. Jiang, Simultaneous enhancement in strength and ductility of Fe50Mn30Co10Cr10 high-entropy alloy via nitrogen alloying, J. Mater. Sci. Technol. 65 (2021) 210–215, https://doi.org/10.1016/j.jmst.2020.04.072.

[5] Z. Li, K.G. Pradeep, Y. Deng, D. Raabe, C.C. Tasan, Metastable high-entropy dual-phase alloys overcome the strength–ductility trade-off, Nature 534 (2016) 227–230, https://doi.org/10.1038/nature17981.

[6] S.S. Nene, K. Liu, M. Frank, R.S. Mishra, R.E. Brennan, K.C. Cho, Z. Li, D. Raabe, Enhanced strength and ductility in a friction stir processing engineered dual phase high entropy alloy, Sci. Rep. 7 (2017) 1–7, https://doi.org/10.1038/s41598-017-16509-9.

[7] Z. Li, D. Raabe, Strong and ductile non-equiatomic high-entropy alloys: design, processing, microstructure, and mechanical properties, JOM 69 (2017) 2099–2106, https://doi.org/10.1007/s11837-017-2540-2.

[8] Z. Li, C.C. Tasan, H. Springer, B. Gault, D. Raabe, Interstitial atoms enable joint twinning and transformation induced plasticity in strong and ductile high-entropy alloys, Sci. Rep. 7 (2017) 1–7, https://doi.org/10.1038/srep40704.

[9] J. Su, X. Wu, D. Raabe, Z. Li, Deformation-driven bidirectional transformation promotes bulk nanostructure formation in a metastable interstitial high entropy alloy, Acta Mater. 167 (2019) 23–39, https://doi.org/10.1016/j.actamat.2019.01.030.

[10] D. Raabe, Z. Li, D. Ponge, Metastability alloy design, MRS Bull. 44 (2019) 266–272, https://doi.org/10.1557/mrs.2019.72.

[11] J. Su, D. Raabe, Z. Li, Hierarchical microstructure design to tune the mechanical behavior of an interstitial TRIP-TWIP high-entropy alloy, Acta Mater. 163 (2019) 40–54, https://doi.org/10.1016/j.actamat.2018.10.017.

[12] X. Wu, D. Mayweg, D. Ponge, Z. Li, Microstructure and deformation behavior of two TWIP/TRIP high entropy alloys upon grain refinement, Mater. Sci. Eng. A 802 (2021), 140661, https://doi.org/10.1016/j.msea.2020.140661.

[13] S.S. Nene, M. Frank, K. Liu, S. Sinha, R.S. Mishra, B. McWilliams, K.C. Cho, Reversed strength-ductility relationship in microstructurally flexible high entropy alloy, Scr. Mater. 154 (2018) 163–167, https://doi.org/10.1016/j.scriptamat.2018.05.043.

[14] S.S. Nene, M. Frank, K. Liu, R.S. Mishra, B.A. McWilliams, K.C. Cho, Extremely high strength and work hardening ability in a metastable high entropy alloy, Sci. Rep. 8 (2018) 1–8, https://doi.org/10.1038/s41598-018-28383-0.

[15] S. Sinha, S.S. Nene, M. Frank, K. Liu, R.A. Lebensohn, R.S. Mishra, Deformation mechanisms and ductile fracture characteristics of a friction stir processed transformative high entropy alloy, Acta Mater. 184 (2020) 164–178, https://doi.org/10.1016/j.actamat.2019.11.056.

[16] S. Palanivel, A. Arora, K.J. Doherty, R.S. Mishra, A framework for shear driven dissolution of thermally stable particles during friction stir welding and processing, Mater. Sci. Eng. A 678 (2016) 308–314, https://doi.org/10.1016/j.msea.2016.10.015.

[17] M. Frank, Y. Chen, S.S. Nene, S. Sinha, K. Liu, K. An, R.S. Mishra, Investigating the deformation mechanisms of a highly metastable high entropy alloy using in-situ neutron diffraction, Mater. Today Commun. 23 (2020) 100858, https://doi.org/10.1016/j.mtcomm.2019.100858.

[18] S.S. Nene, S. Sinha, M. Frank, K. Liu, R.S. Mishra, B.A. McWilliams, K.C. Cho, Unexpected strength–ductility response in an annealed, metastable, high-entropy alloy, Appl. Mater. Today 13 (2018) 198–206, https://doi.org/10.1016/j.apmt.2018.09.002.

[19] F. Kies, P. Köhnen, M.B. Wilms, F. Brasche, K.G. Pradeep, A. Schwedt, S. Richter, A. Weisheit, J.H. Schleifenbaum, C. Haase, Design of high-manganese steels for additive manufacturing applications with energy-absorption functionality, Mater. Des. 160 (2018) 1250–1264, https://doi.org/10.1016/j.matdes.2018.10.051.

[20] Z. Li, F. Körmann, B. Grabowski, J. Neugebauer, D. Raabe, Ab initio assisted design of quinary dual-phase high-entropy alloys with transformation-induced plasticity, Acta Mater. 136 (2017) 262–270, https://doi.org/10.1016/j.actamat.2017.07.023.

[21] Z. Li, C.C. Tasan, K.G. Pradeep, D. Raabe, A TRIP-assisted dual-phase high-entropy alloy: grain size and phase fraction effects on deformation behavior, Acta Mater. 131 (2017) 323–335, https://doi.org/10.1016/j.actamat.2017.03.069.

[22] M.H. Yoo, Slip, twinning, and fracture in hexagonal close-packed metals, MTA 12 (1981) 409–418, https://doi.org/10.1007/BF02648537.

[23] A. Chapuis, J.H. Driver, Temperature dependency of slip and twinning in plane strain compressed magnesium single crystals, Acta Mater. 59 (2011) 1986–1994, https://doi.org/10.1016/j.actamat.2010.11.064.

[24] E.J. Mittemeijer, U. Welzel, Diffraction Line-Profile Analysis, in: Modern Diffraction Methods, John Wiley & Sons, Ltd, n.d.: pp. 87–126. https://doi.org/10.1002/9783527649884.ch4.

[25] S. Van Petegem, A. Guitton, M. Dupraz, A. Bollhalder, K. Sofinowski, M. V. Upadhyay, H. Van Swygenhoven, A miniaturized biaxial deformation rig for in

[26] situ mechanical testing, Exp. Mech. 57 (2017) 569–580, https://doi.org/10.1007/s11340-016-0244-0.

[26] F. Bachmann, R. Hielscher, H. Schaeben, Texture analysis with MTEX – free and open source software toolbox, Solid State Phenom. 160 (2010) 63–68, https://doi.org/10.4028/www.scientific.net/SSP.160.63.

[27] W.-N. Hsu, E. Polatidis, M. Šmíd, S. Van Petegem, N. Casati, H. Van Swygenhoven, Deformation and degradation of superelastic NiTi under multiaxial loading, Acta Mater. 167 (2019) 149–158, https://doi.org/10.1016/j.actamat.2019.01.047.

[28] A.P. Hammersley, S.O. Svensson, M. Hanfland, A.N. Fitch, D. Hausermann, Two-dimensional detector software: from real detector to idealised image or two-theta scan, High. Press. Res. 14 (1996) 235–248, https://doi.org/10.1080/08957959608201408.

[29] B.H. Toby, R.B.Von Dreele, GSAS-II: the genesis of a modern open-source all purpose crystallography software package, J. Appl. Cryst. 46 (2013) 544–549, https://doi.org/10.1107/S0021889813003531.

[30] B.C. De Cooman, Y. Estrin, S.K. Kim, Twinning-induced plasticity (TWIP) steels, Acta Mater. 142 (2018) 283–362, https://doi.org/10.1016/j.actamat.2017.06.046.

[31] Z.C. Cordero, B.E. Knight, C.A. Schuh, Six decades of the Hall–Petch effect – a survey of grain-size strengthening studies on pure metals, Int. Mater. Rev. 61 (2016) 495–512, https://doi.org/10.1080/09506608.2016.1191808.

[32] Z. Sun, S. Van Petegem, A. Cervellino, K. Durst, W. Blum, H. Van Swygenhoven, Dynamic recovery in nanocrystalline Ni, Acta Mater. 91 (2015) 91–100, https://doi.org/10.1016/j.actamat.2015.03.033.

[33] J.F. Nye, Some geometrical relations in dislocated crystals, Acta Metall. 1 (1953) 153–162, https://doi.org/10.1016/0001-6160(53)90054-6.

[34] S. Martin, C. Ullrich, D. Rafaja, Deformation of austenitic CrMnNi TRIP/TWIP steels: nature and role of the ε−martensite, Mater. Today Proc. 2 (2015) S643–S646, https://doi.org/10.1016/j.matpr.2015.07.366.

[35] E. Polatidis, W.-N. Hsu, M. Šmíd, T. Panzner, S. Chakrabarty, P. Pant, H. Van Swygenhoven, Suppressed martensitic transformation under biaxial loading in low stacking fault energy metastable austenitic steels, Scr. Mater. 147 (2018) 27–32, https://doi.org/10.1016/j.scriptamat.2017.12.026.

[36] S.F. Liu, Y. Wu, H.T. Wang, W.T. Lin, Y.Y. Shang, J.B. Liu, K. An, X.J. Liu, H. Wang, Z.P. Lu, Transformation-reinforced high-entropy alloys with superior mechanical properties via tailoring stacking fault energy, J. Alloy. Compd. 792 (2019) 444–455, https://doi.org/10.1016/j.jallcom.2019.04.035.

[37] M. Naeem, H. He, F. Zhang, H. Huang, S. Harjo, T. Kawasaki, B. Wang, S. Lan, Z. Wu, F. Wang, Y. Wu, Z. Lu, Z. Zhang, C.T. Liu, X.-L. Wang, Cooperative deformation in high-entropy alloys at ultralow temperatures, Sci. Adv. 6 (2020), https://doi.org/10.1126/sciadv.aax4002.

[38] Y. Bu, Z. Li, J. Liu, H. Wang, D. Raabe, W. Yang, Nonbasal slip systems enable a strong and ductile hexagonal-close-packed high-entropy phase, Phys. Rev. Lett. 122 (2019), 075502, https://doi.org/10.1103/PhysRevLett.122.075502.

[39] S. Van Petegem, J. Wagner, T. Panzner, M.V. Upadhyay, T.T.T. Trang, H. Van Swygenhoven, In-situ neutron diffraction during biaxial deformation, Acta Mater. 105 (2016) 404–416, https://doi.org/10.1016/j.actamat.2015.12.015.

[40] J. Čapek, J. Stráská, B. Clausen, K. Máthis, Twinning evolution as a function of loading direction in magnesium, Acta Phys. Pol. A 128 (2015) 762–765, https://doi.org/10.12693/APhysPolA.128.762.

[41] S. Fu, H. Bei, Y. Chen, T.K. Liu, D. Yu, K. An, Deformation mechanisms and work-hardening behavior of transformation-induced plasticity high entropy alloys by in -situ neutron diffraction, Mater. Res. Lett. 6 (2018) 620–626, https://doi.org/10.1080/21663831.2018.1523239.

[42] H. Zhang, A. Jérusalem, E. Salvati, C. Papadaki, K.S. Fong, X. Song, A. M. Korsunsky, Multi-scale mechanisms of twinning-detwinning in magnesium alloy AZ31B simulated by crystal plasticity modeling and validated via in situ synchrotron XRD and in situ SEM-EBSD, Int. J. Plast. 119 (2019) 43–56, https://doi.org/10.1016/j.ijplas.2019.02.018.

[43] S. Sinha, S.S. Nene, M. Frank, K. Liu, P. Agrawal, R.S. Mishra, On the evolving nature of c/a ratio in a hexagonal close-packed epsilon martensite phase in transformative high entropy alloys, Sci. Rep. 9 (2019) 1–14, https://doi.org/10.1038/s41598-019-49904-5.

[44] P. Chen, F. Wang, J. Ombogo, B. Li, Formation of 60° ⟨011¯0⟩ boundaries between {101¯2} twin variants in deformation of a magnesium alloy, Mater. Sci. Eng. A 739 (2019) 173–185, https://doi.org/10.1016/j.msea.2018.10.029.

[45] M. Wang, Z. Li, D. Raabe, In-situ SEM observation of phase transformation and twinning mechanisms in an interstitial high-entropy alloy, Acta Mater. 147 (2018) 236–246, https://doi.org/10.1016/j.actamat.2018.01.036.

[46] K. Sofinowski, T. Panzner, M. Kubenova, J. Čapek, S. Van Petegem, H. Van Swygenhoven, In situ tension-tension strain path changes of cold-rolled Mg AZ31B, Acta Mater. 164 (2019) 135–152, https://doi.org/10.1016/j.actamat.2018.10.033.

[47] F. Warchomicka, D. Canelo-Yubero, E. Zehetner, G. Requena, A. Stark, C. Poletti, In-situ synchrotron X-ray diffraction of Ti-6Al-4V during thermomechanical treatment in the beta field, Metals 9 (2019) 862, https://doi.org/10.3390/met9080862.

[48] C.N. Tomé, P.J. Maudlin, R.A. Lebensohn, G.C. Kaschner, Mechanical response of zirconium—I. Derivation of a polycrystal constitutive law and finite element analysis, Acta Mater. 49 (2001) 3085–3096, https://doi.org/10.1016/S1359-6454(01)00190-2.

[49] A.A. Salem, S.R. Kalidindi, R.D. Doherty, Strain hardening regimes and microstructure evolution during large strain compression of high purity titanium, Scr. Mater. 46 (2002) 419–423, https://doi.org/10.1016/S1359-6462(02)00005-2.

[50] Z.S. Basinski, M. Szczerba, M. Niewczas, J.D. Embury, S.J. Basinski, The transformation of slip dislocations during twinning of copper-aluminum alloy crystals, Rev. Metall. Cah. D'Inf. Tech. 94 (1997) 1037–1043, https://doi.org/10.1051/metal/199794091037.

[51] N.M. Della Ventura, S. Kalácska, D. Casari, T.E.J. Edwards, A. Sharma, J. Michler, R. Logé, X. Maeder, {10–12} twinning mechanism during in situ micro-tensile loading of pure Mg: role of basal slip and twin-twin interactions, Mater. Des. 197 (2021), 109206, https://doi.org/10.1016/j.matdes.2020.109206.

[52] Y.Q. Chi, X.H. Zhou, X.G. Qiao, H.G. Brokmeier, M.Y. Zheng, Tension-compression asymmetry of extruded Mg-Gd-Y-Zr alloy with a bimodal microstructure studied by in-situ synchrotron diffraction, Mater. Des. 170 (2019), 107705, https://doi.org/10.1016/j.matdes.2019.107705.

[53] O. Muránsky, D.G. Carr, M.R. Barnett, E.C. Oliver, P. Šittner, Investigation of deformation mechanisms involved in the plasticity of AZ31 Mg alloy: in situ neutron diffraction and EPSC modelling, Mater. Sci. Eng. A 496 (2008) 14–24, https://doi.org/10.1016/j.msea.2008.07.031.

[54] H. Wang, P.D. Wu, C.N. Tomé, J. Wang, Study of lattice strains in magnesium alloy AZ31 based on a large strain elastic-viscoplastic self-consistent polycrystal model, Int. J. Solids Struct. 49 (2012) 2155–2167, https://doi.org/10.1016/j.ijsolstr.2012.04.026.

[55] T.B. Britton, F.P.E. Dunne, A.J. Wilkinson, On the mechanistic basis of deformation at the microscale in hexagonal close-packed metals, Proc. R. Soc. A 471 (2015), 20140881, https://doi.org/10.1098/rspa.2014.0881.

[56] L. Wang, Z. Zheng, H. Phukan, P. Kenesei, J.-S. Park, J. Lind, R.M. Suter, T. R. Bieler, Direct measurement of critical resolved shear stress of prismatic and basal slip in polycrystalline Ti using high energy X-ray diffraction microscopy, Acta Mater. 132 (2017) 598–610, https://doi.org/10.1016/j.actamat.2017.05.015.